applied optics

Linear depolarization of lidar returns by aged smoke particles

Michael I. Mishchenko,[1,*] Janna M. Dlugach,[2] and Li Liu[3]

[1]NASA Goddard Institute for Space Studies, 2880 Broadway, New York, New York 10025, USA
[2]Main Astronomical Observatory of the National Academy of Sciences of Ukraine, 27 Zabolotny Str., 03680, Kyiv, Ukraine
[3]Columbia University and NASA Goddard Institute for Space Studies, 2880 Broadway, New York, New York 10025, USA
*Corresponding author: michael.i.mishchenko@nasa.gov

Received 2 September 2016; revised 31 October 2016; accepted 2 November 2016; posted 2 November 2016 (Doc. ID 275157); published 5 December 2016

We use the numerically exact (superposition) T-matrix method to analyze recent measurements of the backscattering linear depolarization ratio (LDR) for a plume of aged smoke at lidar wavelengths ranging from 355 to 1064 nm. We show that the unique spectral dependence of the measured LDRs can be modeled, but only by assuming expressly nonspherical morphologies of smoke particles containing substantial amounts of nonabsorbing (or weakly absorbing) refractory materials such as sulfates. Our results demonstrate that spectral backscattering LDR measurements can be indicative of the presence of morphologically complex smoke particles, but additional (e.g., passive polarimetric or bistatic lidar) measurements may be required for a definitive characterization of the particle morphology and composition. © 2016 Optical Society of America

OCIS codes: (290.5850) Scattering, particles; (290.1090) Aerosol and cloud effects; (290.1350) Backscattering; (290.5855) Scattering, polarization.

https://doi.org/10.1364/AO.55.009968

1. INTRODUCTION

Soot particles represent an important category of tropospheric aerosols causing a direct radiative forcing of climate, affecting cloud formation, and reducing the albedo of ice and snow surfaces [1–8]. It is therefore essential to determine the global distribution of soot and soot-containing aerosols and their microphysical properties from satellite observations.

It is widely recognized that one of the most potent remote-sensing tools for the optical characterization of morphologically complex particulates is the measurement of the linear depolarization ratio (LDR) with backscattering lidars [9–20]. Until quite recently, it had generally been believed that strong absorption of light by black carbon causes very small (and thereby hardly useful) LDR values. However, the observations of a smoke plume with the NASA Langley High Spectral Resolution Lidar-2 (HSRL-2) reported by Burton *et al.* [20] revealed highly unusual LDR values reaching 0.2 at the 355-nm lidar wavelength. Furthermore, the measured spectral dependence of the smoke LDR was distinctly different from that of dust aerosols.

The initial theoretical analysis of the observed LDR values in [20] (based on the results of [21]) was promising but somewhat inconclusive. Yet it appears to be important to demonstrate explicitly that specific complex morphologies of soot-containing aerosols can indeed reproduce the observed spectral dependence of the LDR and thereby confirm the potential of lidar depolarization measurements to identify and characterize smoke particles. This demonstration would be especially appropriate given the anticipated flight of a polarization lidar as part of the planned NASA Aerosol–Cloud–Ecosystem space mission.

Given the extreme complexity of the depolarization scattering phenomenon, it is imperative to analyze the LDR measurements reported in [20] on the basis of a first-principles scattering methodology involving a direct computer solver of the macroscopic Maxwell equations [22–24]. In this paper, we use for this purpose the highly efficient and numerically exact (superposition) T-matrix method.

2. LIDAR MEASUREMENTS

The real-valued so-called normalized Stokes scattering matrix typical of randomly oriented aerosol particles has the following block-diagonal structure [25,26]:

$$\tilde{\mathbf{F}}(\Theta) = \begin{bmatrix} a_1(\Theta) & b_1(\Theta) & 0 & 0 \\ b_1(\Theta) & a_2(\Theta) & 0 & 0 \\ 0 & 0 & a_3(\Theta) & b_2(\Theta) \\ 0 & 0 & -b_2(\Theta) & a_4(\Theta) \end{bmatrix}, \quad (1)$$

where Θ is the scattering angle and the (1, 1) element (conventionally referred to as the phase function) is normalized according to

Table 1. Measured Spectral Values of the Linear Depolarization Ratio and Their Ranges [20]

	δ (355 nm)	δ (532 nm)	δ (1064 nm)
Measured	0.203 ± 0.036 (0.017)	0.093 ± 0.015 (0.011)	0.018 ± 0.002 (0.007)
Range	[0.150, 0.256]	[0.067, 0.119]	[0.009, 0.027]

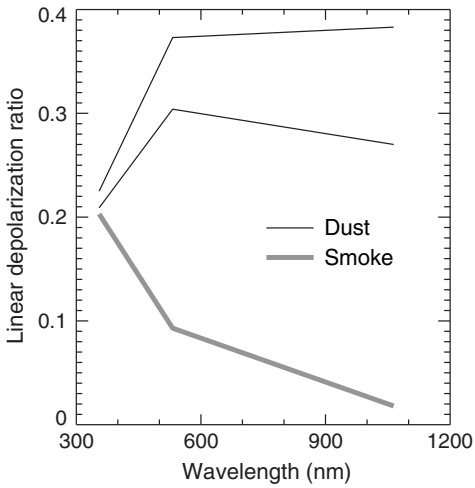

Fig. 1. Spectral dependence of the LDRs observed for dust-dominated aerosol and smoke [20].

$$\frac{1}{2}\int_0^{\pi} \mathrm{d}\Theta a_1(\Theta)\sin\Theta = 1. \tag{2}$$

The LDR is then defined as

$$\delta = \frac{a_1(180°) - a_2(180°)}{a_1(180°) + a_2(180°)}. \tag{3}$$

The LDR values measured by Burton *et al.* [20] at the three NASA HSRL-2 wavelengths (355, 532, and 1064 nm) are summarized in Table 1. The measured values are reported as mean ± one standard deviation for the sample, while systematic measurement uncertainties from the NASA HSRL-2 are given in parentheses. Also shown are the resulting approximate ranges of the measured LDR values, each calculated as the mean ± the sum of the systematic measurement uncertainty and one standard deviation. The observations were performed during the Colorado deployment of the DISCOVER-AQ (Deriving Information on Surface Conditions from Column and Vertically Resolved Observations Relevant to Air Quality) field mission on 27 July 2014, and pertain to a plume of wildfire smoke situated at a ~8-km altitude. Figure 1 reveals indeed that the spectral dependence of the smoke LDR is distinctly different from that observed typically for dust-dominated aerosol.

3. MODEL PARTICLE MORPHOLOGIES

It has been well documented that the morphology of smoke particulates can change dramatically during their aging [27–33]. The LDR values computed for fluffy and compact aggregates consisting of pure black-carbon monomers are very small (typically smaller than a few percent [17,34,35]) and cannot explain the observed values indicated in Table 1. Therefore, we need to consider alternative particulate morphologies lacking spherical symmetry and involving significant amounts of a nonabsorbing (or weakly absorbing) refractory material.

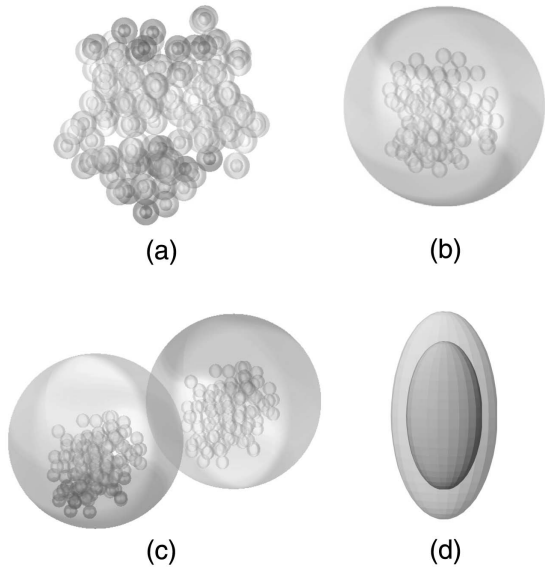

Fig. 2. Model morphologies of soot-containing particulates.

One such morphology considered in [21] is a spherical sulfate host with a partially imbedded soot aggregate. Four other model morphologies of aged soot-containing particulates are shown in Fig. 2. The so-called closed-cell morphology depicted in Fig. 2(a) (hereinafter model 1) represents the process of accumulation of a refractory material around individual soot monomers constituting a compact cluster formed after the collapse of the initial fluffy soot aggregate. Figure 2(b) shows a spherical sulfate aerosol hosting a completely imbedded compact soot cluster (hereinafter model 2). Figure 2(c) shows two spherical sulfate particles in contact, each encapsulating a compact soot aggregate (hereinafter model 3). Finally, Fig. 2(d) shows a concentric core–mantle spheroid intended to model a high-density aspherical soot core enveloped by a layer of sulfate material (hereinafter model 4). The scattering properties of models 1–3 were computed using the random-orientation superposition T-matrix method developed by Mackowski [36], while those of model 4 were quantified using the random-orientation T-matrix program by Quirantes [37].

4. NUMERICAL RESULTS

Extensive T-matrix computations for various realizations of model 2 have shown that this morphology causes LDR values too small to reproduce the observed depolarization of lidar returns by smoke particulates. Indeed, linear depolarization is typically ~1% or smaller at all wavelengths. The most likely explanation of this finding is that the outer boundary of such particles is spherical and dominates (i.e., suppresses) the resulting LDRs. Therefore, we will exclude model 2 from the following discussion.

A. Model 1

It has been demonstrated in [34,38] that the overall morphology of a random soot aggregate is well represented by a fractal cluster parameterized by the following statistical scaling law:

$$N = k_0 \left(\frac{R_g}{a}\right)^{D_f}, \tag{4}$$

where a is the monomer mean radius, k_0 is the fractal prefactor, D_f is the fractal dimension, N is the number of monomers in the cluster, and R_g is the radius of gyration. The latter is a measure of the overall radius of the aggregate and is defined by

$$R_g^2 = \frac{1}{N}\sum_{i=1}^{N} r_i^2, \tag{5}$$

where r_i is the distance of the ith monomer to the cluster's center of mass. The fractal dimension serves as a quantitative measure of the aggregate morphology. D_f values close to 3 represent densely packed aggregates, whereas chain-like branched clusters can have significantly smaller values. The fractal prefactor is also related to the state of compactness of a fractal particle in that for a fixed fractal dimension the packing density tends to be smaller for smaller k_0.

Consistent with the previous discussion of model 1, we will assume that each monomer in the aggregate shown in Fig. 2(a) consists of a spherical soot core with a radius a_s located in the center of a spherical sulfate host with a radius a. The refractive indices of soot at the three lidar wavelengths were estimated according to Eqs. (19a) and (19b) of [39] and are as follows: $1.66284 + 0.715235i$ at 355 nm, $1.73156 + 0.600028i$ at 532 nm, and $1.81895 + 0.590511i$ at 1064 nm. The corresponding sulfate refractive indices were interpolated from the tabulated values at 50% relative humidity in [40] and are as follows: 1.3813 at 355 nm, 1.3684 at 532 nm, and 1.3595 at 1064 nm.

Our T-matrix results show that model 1 is capable of reproducing the observed spectral dependence of the LDR. As an example, in Table 2 we list the LDR values computed for 10 random realizations of the model-1 morphology with the following fixed fractal parameters: $k_0 = 1.2$, $D_f = 2.6$, $N = 125$, $a_s = 20$ nm, and $a = 6a_s$. It can be seen indeed that the LDR values in Table 2 follow the observed spectral trend and are approximately consistent with the ranges of the measured LDRs in Table 1.

Table 2. T-matrix Results for 10 Fractal-Parameter-Equivalent Realizations of Model 1

Realization	δ (355 nm)	δ (532 nm)	δ (1064 nm)
1	0.222	0.056	0.015
2	0.238	0.060	0.021
3	0.237	0.066	0.012
4	0.229	0.060	0.015
5	0.252	0.062	0.013
6	0.224	0.068	0.015
7	0.243	0.054	0.012
8	0.237	0.055	0.010
9	0.239	0.072	0.013
10	0.226	0.056	0.014

Table 3. T-matrix Results for Seven Versions of Model 1

a/a_s	δ (355 nm)	δ (532 nm)	δ (1064 nm)
5.7	0.289	0.054	0.015
5.8	0.274	0.057	0.015
5.9	0.259	0.060	0.015
6	0.244	0.063	0.016
6.1	0.228	0.067	0.016
6.2	0.212	0.072	0.016
6.3	0.199	0.078	0.016

Similarly, in Table 3 we show the results of T-matrix computations for the same fixed values of the parameters k_0, D_f, N, and a_s, but for seven values of a ranging from $5.7a_s$ to $6.3a_s$. Again the resulting LDRs, at least those for $a \geq 6a_s$, are largely consistent with Table 1.

B. Model 3

Table 4 summarizes the results of T-matrix computations for 10 random realizations of the model-3 morphology, assuming that each spherical sulfate host encapsulates a soot fractal aggregate with $k_0 = 1.2$, $D_f = 2.6$, $N = 125$, and $a_s = 20$ nm. The host radius is 232 nm, and the corresponding soot volume fraction is 0.08. The soot and sulfate refractive indices are the same as in the preceding subsection. Table 5 is similar but illustrates the sensitivity of the modeled LDRs to the host radius when the soot inclusions remain the same. Again, most of these model-3 T-matrix results are consistent with the LDR ranges in Table 1.

C. Model 4

Finally, Tables 6 and 7 summarize select T-matrix results for the model-4 morphology. The overall shape of the core–mantle spheroidal particle is characterized by the axis ratio $\varepsilon = a/b$, where b is the rotational (vertical) axis of the corresponding

Table 4. T-matrix Results for 10 Fractal-Parameter-Equivalent Realizations of Model 3

Realization	δ (355 nm)	δ (532 nm)	δ (1064 nm)
1	0.225	0.093	0.016
2	0.242	0.105	0.018
3	0.220	0.097	0.017
4	0.264	0.110	0.019
5	0.267	0.107	0.019
6	0.232	0.101	0.017
7	0.252	0.102	0.018
8	0.235	0.095	0.016
9	0.264	0.108	0.019
10	0.262	0.109	0.019

Table 5. T-matrix Results for Six Versions of Model 3

Host radius (nm)	δ (355 nm)	δ (532 nm)	δ (1064 nm)
230	0.276	0.091	0.017
232	0.248	0.103	0.017
234	0.224	0.116	0.018
236	0.202	0.130	0.018
368	0.196	0.113	0.024

Table 6. *T*-matrix Model-4 Results for $m_{soot} = 1.75 + 0.435i$

R_{eff} (nm)	R_{core} (nm)	ε	δ (355 nm)	δ (532 nm)	δ (1064 nm)
450	150	1.2	0.241	0.092	0.011
670	200	1.1	0.197	0.090	0.008
640	250	1.1	0.147	0.076	0.015
600	250	1.15	0.228	0.127	0.027
550	150	0.9	0.256	0.089	0.009
550	250	0.9	0.208	0.110	0.022

Table 7. *T*-matrix Model-4 Results for $m_{soot} = 1.67 + 0.27i$

R_{eff} (nm)	R_{core} (nm)	ε	δ (355 nm)	δ (532 nm)	δ (1064 nm)
470	150	1.2	0.244	0.097	0.008
550	200	1.15	0.207	0.099	0.013
510	250	1.15	0.164	0.110	0.015
600	250	1.15	0.225	0.118	0.018
550	250	0.9	0.204	0.094	0.014
600	300	0.9	0.226	0.132	0.027

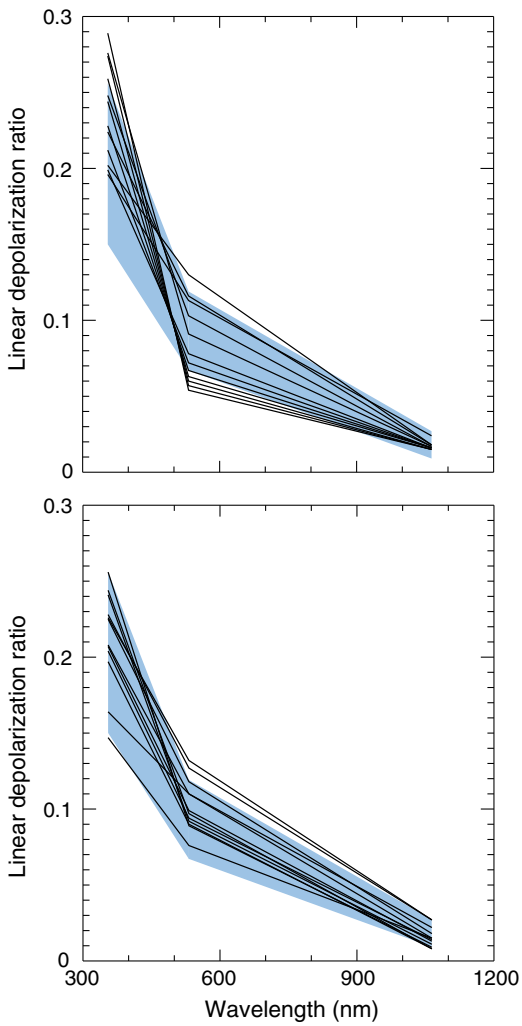

Fig. 3. Graphical summaries of Tables 3 and 5 (upper panel) and Tables 6 and 7 (lower panel). The shaded area shows the range of measurement uncertainty according to Table 1.

ellipse and a is the horizontal axis. The axis ratio is assumed to be the same for both the soot core and the sulfate shell. To suppress the effect of scattering resonances on the modeled LDRs, each result is averaged over a narrow power law distribution of shell sizes while assuming that the core remains the same. Accordingly, R_{eff} in Tables 6 and 7 is the effective equal-volume-sphere radius of the entire core–mantle particle, and R_{core} is the monodisperse equal-volume-sphere radius of the soot core. The effective variance of the power law distribution [41] is fixed at 0.01. The sulfate and soot refractive indices are assumed to be wavelength-independent. The former is fixed at 1.44, while the latter is $m_{soot} = 1.75 + 0.435i$ in Table 6 and $m_{soot} = 1.67 + 0.27i$ in Table 7. Again, the reader can verify that the majority of modeled LDR values in these tables are consistent with the LDR ranges given in Table 1.

5. DISCUSSION

The main objective of this paper is rather limited: to demonstrate that complex morphologies of aged soot-containing aerosols can reproduce the unique spectral dependence of linear depolarization observed for an aged smoke plume by Burton *et al.* [20] (see Fig. 3). Perhaps the most important outcome of our study is that achieving this objective requires the use of expressly nonspherical overall morphologies containing substantial amounts of nonabsorbing (or weakly absorbing) refractory materials (referred to generically as "sulfates"). We have shown that the measured spectral LDR values can be reproduced by a range of model morphologies and a range of model soot and sulfate refractive indices. We leave it up to the experts in aerosol physics and chemistry to discuss which morphological models and/or refractive indices are more or less realistic. It is obvious, however, that spectral LDR measurements can indeed be used to identify the presence of morphologically complex smoke particles, even though additional observations (e.g., with a passive polarimetrer [42] or a bistatic lidar [43,44]) may be required to narrow down the plausible ranges of particle morphology (including size) and composition.

Funding. National Aeronautics and Space Administration (NASA) ACE Project, NASA Remote Sensing Theory Program; National Academy of Sciences of Ukraine Main Astronomical Observatory GRAPE/GPU/GRID Computing Cluster Project.

Acknowledgment. We thank Daniel Mackowski and Arturo Quirantes for making their *T*-matrix programs publicly available and Nadia Zakharova for help with graphics. We also acknowledge insightful discussions with W. Patrick Arnott, Sharon Burton, Michael Kahnert, and Igor Veselovskii.

REFERENCES

1. P. Chýlek, G. B. Lesins, G. Videen, J. G. D. Wong, R. G. Pinnick, D. Ngo, and J. D. Klett, "Black carbon and absorption of solar radiation by clouds," J. Geophys. Res. **101**, 23365–23371 (1996).
2. A. S. Ackerman, O. B. Toon, D. E. Stevens, A. J. Heymsfield, V. Ramanathan, and E. J. Welton, "Reduction of tropical cloudiness by soot," Science **288**, 1042–1047 (2000).

3. J. Hansen, T. Bond, B. Cairns, H. Gaeggler, B. Liepert, T. Novakov, and B. Schichtel, "Carbonaceous aerosols in the industrial era," Eos Trans. Am. Geophys. Union **85**, 241 (2004).
4. J. Hansen and L. Nazarenko, "Soot climate forcing via snow and ice albedos," Proc. Natl. Acad. Sci. USA **101**, 423–428 (2004).
5. V. Ramanathan and G. Carmichael, "Global and regional climate changes due to black carbon," Nat. Geosci. **1**, 221–227 (2008).
6. H. Moosmüller, R. K. Chakrabarty, and W. P. Arnott, "Aerosol light absorption and its measurement: a review," J. Quant. Spectrosc. Radiat. Transfer **110**, 844–878 (2009).
7. D. Koch and A. D. Del Genio, "Black carbon absorption effects on cloud cover: review and synthesis," Atmos. Chem. Phys. **10**, 7685–7696 (2010).
8. T. C. Bond, S. J. Doherty, D. W. Fahey, P. M. Forster, T. Berntsen, B. J. DeAngelo, M. G. Flanner, S. Ghan, B. Karcher, D. Koch, S. Kinne, Y. Kondo, P. K. Quinn, M. C. Sarofim, M. G. Schultz, M. Schulz, C. Venkataraman, H. Zhang, S. Zhang, N. Bellouin, S. K. Guttikunda, P. K. Hopke, M. Z. Jacobson, J. W. Kaiser, Z. Klimont, U. Lohmann, J. P. Schwarz, D. Shindell, T. Storelvmo, S. G. Warren, and C. S. Zender, "Bounding the role of black carbon in the climate system: a scientific assessment," J. Geophys. Res. Atmos. **118**, 5380–5552 (2013).
9. K. Sassen, "The polarization lidar technique for cloud research: a review and current assessment," Bull. Am. Meteorol. Soc. **72**, 1848–1866 (1991).
10. M. I. Mishchenko and J. W. Hovenier, "Depolarization of light backscattered by randomly oriented nonspherical particles," Opt. Lett. **20**, 1356–1358 (1995).
11. T. Murayama, H. Okamoto, N. Kaneyasu, H. Kamataki, and K. Miura, "Application of lidar depolarization measurement in the atmospheric boundary layer: effects of dust and sea-salt particles," J. Geophys. Res. **104**, 31781–31792 (1999).
12. K. Sassen, "Polarization in lidar," in *Lidar: Range-Resolved Optical Remote Sensing of the Atmosphere*, C. Weitkamp, ed. (Springer, 2005), pp. 355–397.
13. V. Freudenthaler, M. Esselborn, M. Wiegner, B. Heese, M. Tesche, A. Ansmann, D. Müller, D. Althausen, M. Wirth, A. Fix, G. Ehret, P. Knippertz, C. Toledano, J. Gasteiger, M. Garhammer, and M. Seefeldner, "Depolarization ratio profiling at several wavelengths in pure Saharan dust during SAMUM 2006," Tellus B **61**, 165–179 (2009).
14. D. M. Winker, M. A. Vaughan, A. Omar, Y. Hu, K. A. Powell, Z. Liu, W. H. Hunt, and S. A. Young, "Overview of the CALIPSO mission and CALIOP data processing algorithms," J. Atmos. Ocean. Technol. **26**, 2310–2323 (2009).
15. T. Nishizawa, N. Sugimoto, I. Matsui, A. Shimizu, and H. Okamoto, "Algorithms to retrieve optical properties of three component aerosols from two-wavelength backscatter and one-wavelength polarization lidar measurements considering nonsphericity of dust," J. Quant. Spectrosc. Radiat. Transfer **112**, 254–267 (2011).
16. S. P. Burton, R. A. Ferrare, C. A. Hostetler, J. W. Hair, R. R. Rogers, M. D. Obland, C. F. Butler, A. L. Cook, D. B. Harper, and K. D. Froyd, "Aerosol classification using airborne high spectral resolution lidar measurements—methodology and examples," Atmos. Meas. Tech. **5**, 73–98 (2012).
17. M. I. Mishchenko, L. Liu, and D. W. Mackowski, "T-matrix modeling of linear depolarization by morphologically complex soot and soot-containing aerosols," J. Quant. Spectrosc. Radiat. Transfer **123**, 135–144 (2013).
18. N. Sugimoto, T. Nishizawa, A. Shimizu, I. Matsui, and H. Kobayashi, "Detection of internally mixed Asian dust with air pollution aerosols using a polarization optical particle counter and a polarization-sensitive two-wavelength lidar," J. Quant. Spectrosc. Radiat. Transfer **150**, 107–113 (2015).
19. B. Gross, F. Moshary, and M. Arend, eds., *27th International Laser Radar Conference (ILRC 27)*, Vol. **119** of EPJ Web of Conferences (2016), http://www.epj-conferences.org.
20. S. P. Burton, J. W. Hair, M. Kahnert, R. A. Ferrare, C. A. Hostetler, A. L. Cook, D. B. Harper, T. A. Berkoff, S. T. Seaman, J. E. Collins, M. A. Fenn, and R. R. Rogers, "Observations of the spectral dependence of linear particle depolarization ratio of aerosols using NASA Langley airborne high spectral resolution lidar," Atmos. Chem. Phys. **15**, 13453–13473 (2015), Corrigendum: http://www.atmos-chem-phys.net/15/13453/2015/acp-15-13453-2015-corrigendum.pdf.
21. M. Kahnert, T. Nousiainen, H. Lindqvist, and M. Ebert, "Optical properties of light absorbing carbon aggregates mixed with sulfate: assessment of different model geometries for climate forcing calculations," Opt. Express **20**, 10042–10058 (2012).
22. M. I. Mishchenko, W. J. Wiscombe, J. W. Hovenier, and L. D. Travis, "Overview of scattering by nonspherical particles," in *Light Scattering by Nonspherical Particles: Theory, Measurements, and Applications*, M. I. Mishchenko, J. W. Hovenier, and L. D. Travis, eds. (Academic, 2000), pp. 29–60.
23. F. M. Kahnert, "Numerical methods in electromagnetic scattering theory," J. Quant. Spectrosc. Radiat. Transfer **79–80**, 775–824 (2003).
24. M. Kahnert, "Numerical solutions of the macroscopic Maxwell equations for scattering by non-spherical particles: a tutorial review," J. Quant. Spectrosc. Radiat. Transfer **178**, 22–37 (2016).
25. H. C. van de Hulst, *Light Scattering by Small Particles* (Wiley, 1957).
26. M. I. Mishchenko, *Electromagnetic Scattering by Particles and Particle Groups: An Introduction* (Cambridge University, 2014).
27. R. K. Chakrabarty, H. Moosmüller, M. A. Garro, W. P. Arnott, J. Walker, R. A. Susott, R. E. Babbitt, C. E. Wold, E. N. Lincoln, and W. M. Hao, "Emissions from the laboratory combustion of wildland fuels: particle morphology and size," J. Geophys. Res. **111**, D07204 (2006).
28. R. Zhang, A. F. Khalizov, J. Pagels, D. Zhang, H. Xue, and P. H. McMurry, "Variability in morphology, hygroscopicity, and optical properties of soot aerosols during atmospheric processing," Proc. Natl. Acad. Sci. USA **105**, 10291–10296 (2008).
29. K. A. Lewis, W. P. Arnott, H. Moosmüller, R. K. Chakrabarty, C. M. Carrico, S. M. Kreidenweis, D. E. Day, W. C. Malm, A. Laskin, J. L. Jimenez, I. M. Ulbrich, J. A. Huffman, T. B. Onasch, A. Trimborn, L. Liu, and M. I. Mishchenko, "Reduction in biomass burning aerosol light absorption upon humidification: roles of inorganically-induced hygroscopicity, particle collapse, and photoacoustic heat and mass transfer," Atmos. Chem. Phys. **9**, 8949–8966 (2009).
30. K. Adachi, S. H. Chung, and P. R. Buseck, "Shapes of soot aerosol particles and implications for their effects on climate," J. Geophys. Res. **115**, D15206 (2010).
31. S. Ueda, K. Osada, and A. Takami, "Morphological features of soot-containing particles internally mixed with water-soluble materials in continental outflow observed at Cape Hedo, Okinawa, Japan," J. Geophys. Res. **116**, D17207 (2011).
32. S. China, C. Mazzoleni, K. Gorkowski, A. C. Aiken, and M. K. Dubey, "Morphology and mixing state of individual freshly emitted wildfire carbonaceous particles," Nat. Commun. **4**, 2122 (2013).
33. S. China, B. Scarnato, R. C. Owen, B. Zhang, M. T. Ampadu, S. Kumar, K. Dzepina, M. P. Dziobak, P. Fialho, J. A. Perlinger, J. Hueber, D. Helmig, L. R. Mazzoleni, and C. Mazzoleni, "Morphology and mixing state of aged soot particles at a remote marine free troposphere site: implications for optical properties," Geophys. Res. Lett. **42**, 1243–1250 (2015).
34. C. Sorensen, "Light scattering by fractal aggregates: a review," Aerosol Sci. Technol. **35**, 648–687 (2001).
35. A. Bescond, J. Yon, T. Girasole, C. Jouen, C. Rozé, and A. Coppalle, "Numerical investigation of the possibility to determine the primary particle size of fractal aggregates by measuring light depolarization," J. Quant. Spectrosc. Radiat. Transfer **126**, 130–139 (2013).
36. D. W. Mackowski, "A general superposition solution for electromagnetic scattering by multiple spherical domains of optically active media," J. Quant. Spectrosc. Radiat. Transfer **133**, 264–270 (2014).
37. A. Quirantes, "A T-matrix method and computer code for randomly oriented, axially symmetric coated scatterers," J. Quant. Spectrosc. Radiat. Transfer **92**, 373–381 (2005).
38. E. F. Mikhailov, S. S. Vlasenko, and A. A. Kiselev, "Optics and structure of carbonaceous soot aggregates," in *Optics of Nanostructured Materials*, V. A. Markel and T. F. George, eds. (Wiley, 2001), pp. 413–466.
39. H. Chang and T. T. Charalampopoulos, "Determination of the wavelength dependence of refractive indices of flame soot," Proc. R. Soc. London A **430**, 577–591 (1990).

40. M. Hess, P. Koepke, and I. Schult, "Optical properties of aerosols and clouds: the software package OPAC," Bull. Am. Meteorol. Soc. **79**, 831–844 (1998).
41. J. E. Hansen and L. D. Travis, "Light scattering in planetary atmospheres," Space Sci. Rev. **16**, 527–610 (1974).
42. K. Knobelspiesse, B. Cairns, M. Ottaviani, R. Ferrare, J. Hair, C. Hostetler, M. Obland, R. Rogers, J. Redemann, Y. Shinozuka, A. Clarke, S. Freitag, S. Howell, V. Kapustin, and C. McNaughton, "Combined retrievals of boreal forest fire aerosol properties with a polarimeter and lidar," Atmos. Chem. Phys. **11**, 7045–7067 (2011).
43. J. A. Reagan, D. M. Byrne, and B. M. Herman, "Bistatic LIDAR: a tool for characterizing atmospheric particulates: part II—the inverse problem," IEEE Trans. Geosci. Remote Sens. **GE-20**, 236–243 (1982).
44. M. I. Mishchenko, M. D. Alexandrov, B. Cairns, and L. D. Travis, "Multistatic aerosol-cloud lidar in space: a theoretical perspective," J. Quant. Spectrosc. Radiat. Transfer **184**, 180–192 (2016).